RSC Advances

PAPER

Cite this: *RSC Adv.*, 2024, **14**, 1186

Theoretical prediction on the stability, elastic, electronic and optical properties of MAB-phase M_4AlB_4 compounds (M = Cr, Mo, W)†

Yaoping Lu,[a] Titao Li,*[a] Kangjie Li,[b] Derek Hao,[c] Zuxin Chen*[b] and Haizhong Zhang*[a]

This research employs first-principles calculations to address the challenges presented by processing complexity and low damage tolerance in transition metal borides. The study focuses on designing and investigating MAB phase compounds of M_4AlB_4 (M = Cr, Mo, W). We conduct a comprehensive assessment of the stability, phononic, electronic, elastic, and optical properties of Cr_4AlB_4, Mo_4AlB_4, and W_4AlB_4. The calculated results reveal formation enthalpies of −0.516, −0.490, and −0.336 eV per atom for Cr_4AlB_4, Mo_4AlB_4, and W_4AlB_4, respectively. Notably, W_4AlB_4 emerges as a promising precursor material for MABene synthesis, demonstrating exceptional thermal shock resistance. The dielectric constants $\varepsilon_1(0)$ were determined as 126.466, 80.277, and 136.267 for Cr_4AlB_4, Mo_4AlB_4, and W_4AlB_4, respectively. Significantly, W_4AlB_4 exhibits remarkably high reflectivity (>80%) within the wavelength range of 19.84–23.6 nm, making it an ideal candidate for extreme ultraviolet (EUV) reflective coatings. The insights gleaned from this study provide a strong research framework and theoretical guidance for advancing the synthesis of innovative MAB-phase compounds.

Received 14th September 2023
Accepted 11th December 2023

DOI: 10.1039/d3ra06267h

rsc.li/rsc-advances

1. Introduction

Binary transition metal borides (TMBs), represented by OsB_2,[1] ReB_2,[2] CrB[3] and WB,[4] hold promising potential across various domains such as wear-resistant coatings, electrocatalysts, and electrodes. This stems from their extremely high hardness, excellent wear resistance, and distinctive electronic structure.[1–3,5–7] However, the formidable challenges in processing and their limited damage tolerance significantly curtail the broader utilization of TMBs.[3,4] Previous studies have shown that the selective introduction of Al elements into high-hardness TMB materials to forge what are known as "MAB" phase compounds can effectively improve the fracture toughness and damage tolerance of material systems.[8,9] Moreover, certain MAB phase compounds, owning to their superb resistance to thermal shock[10] and high-temperature oxidation,[11,12] are deemed as prime candidates for fabricating hypersonic aircraft and scramjet engines.[13–15]

Structurally, MAB phase compounds arise from the alternate layering of Al atomic layers and TMB layers:[9–12] within the TMB layers, robust B–B bonds (typically <2 Å) and TM–B bonds (typically ~2 Å) coexist, whereas the bonds linking the TMB layers and Al layers, such as TM–Al and Al–B bonds (typically >2 Å), exhibit comparatively lower strength.[16,17] The judicious selection of Poisson's ratio and modulus of elasticity from these crystal structures enables MAB phase compounds to amalgamate the favorable traits of metals-low brittleness and high ductility-with the robust attributes of ceramics, including high hardness and exceptional wear resistance. This amalgamation renders them more amenable to processing and more pragmatic in contrast to conventional TMB phases.[12] Additionally, this unique structure facilitates the facile creation of MBene materials through the corrosion of Al atoms.[3,18] Recently, Zhang *et al.* introduced a novel MAB phase, Cr_4AlB_4 (achieved by incorporating an Al layer into CrB material), enhancing the damage tolerance and thermal shock resistance of CrB.[19]

Considering the formation enthalpy and cohesive energy, Adam Carlsson *et al.* have conducted theoretical calculations on 420 types of MAB phase structures, efficiently screening out more than 40 potentially synthesizable materials.[20] Among these, Mo_4AlB_4, sharing an identical structure with Cr_4AlB_4, also emerges as a viable synthesis candidate. Zhou *et al.* have demonstrated the feasibility of procuring two-dimensional MoB through chemical exfoliation.[21] However, in our assessment, scope remains for refining the existing research, potentially enhance the stability of the MAB phase and minimizing

[a]*Jinjiang Joint Institute of Microelectronics, College of Physics and Information Engineering, Fuzhou University, Fuzhou 350108, China. E-mail: litt69@fzu.edu.cn; haizhong_zhang@fzu.edu.cn*

[b]*School of Semiconductor Science and Technology, South China Normal University, Foshan 528225, China. E-mail: chenzuxin@m.scnu.edu.cn*

[c]*School of Science, RMIT University, Melbourne, VIC 3000, Australia*

† Electronic supplementary information (ESI) available. See DOI: https://doi.org/10.1039/d3ra06267h

possible deviations from real-world outcomes. Furthermore, the current uncertainties surrounding the mechanical and dynamic stability cast doubts about the pragmatic applicability of these materials. Thus, a sole concentration on energy-related aspects is insufficient in appraising the stability of MAB phase compounds.

In this work, we undertook a comprehensive re-evaluation of the stability of Cr_4AlB_4, Mo_4AlB_4, and W_4AlB_4 crystals through first-principles calculations, further exploring their potential applications. Based on the experimental results of Zhang *et al.*[22] and the structural models of Adam Carlsson *et al.*,[20] we performed a rigorous re-optimization of the crystal models for Cr_4AlB_4, Mo_4AlB_4, and W_4AlB_4. This optimization process, incorporating heightened convergence accuracy, was undertaken from multiple vantage points, encompassing formation enthalpy, cohesive energy, mechanical stability, and dynamic stability. Consequently, our investigations substantiate the stable existence of Mo_4AlB_4 and W_4AlB_4 across diverse perspectives. Further investigations have also unveiled that W_4AlB_4 exhibits a reflectance exceeding 80% within the 19.3–23.4 nm range, making as a potential extreme ultraviolet (EUV) reflective coatings. The suitable Poisson's ratio of Mo_4AlB_4 hints at its potential as a material endowed with high damage tolerance. The strategic inclusion of an Al layer within Mo_4AlB_4 and W_4AlB_4 amplifies their potential not only as materials resistant to thermal shocks but also as auspicious precursors for the development of MBene materials.

2. Computational methods

The VASP code,[23,24] was used for first-principles calculations based on Density Functional Theory (DFT)[25–27] in this materials research study. The exchange correlation energy was expressed by the Perdew–Burke–Ernzerhof (PBE) method in the Generalised Gradient Approximation (GGA).[28,29] The configurations of valence electrons for Cr, Mo, W, Al and B were chosen to be [Ar] $3d^5 4s^1$, [Kr]$4d^5 5s^1$, [Xe]$4f^{14} 5d^4 6s^2$, [Ne]$3s^2 3p^1$ and [He]$2s^2 2p^1$, respectively. Structures and energies of the MAB phases were fully optimized in this work. Cutoff energy was set at 750 eV, the Monkhorst–Pack scheme *k*-points mesh separation was 0.03 $Å^{-1}$. The force converge criterion was set to 10^{-6} eV $Å^{-1}$, and the energy was converged to within 10^{-10} eV for the electronic steps. The phonon frequencies were calculated by the finite displacement method, using PHONOPY program, with the cutoff energy and *k*-points were 750 eV and 11 × 2 × 11, respectively.[30]

3. Results and discussions

3.1. Structural properties and phase stability

Compound M_4AlB_4 (M = Cr, Mo, W) crystals have an orthorhombic structure, which belongs to the No. 71-space group (*Immm*),[19,20,22] Fig. 1 exhibited the unit cell of these M_4AlB_4 tetraborides. In this structure, M atoms were located at positions 4h (0, 0.2936, 0) and 4g (0.5, 0.5859, 0), Al atoms were located at positions 2b (0, 0.5, 0.5), B atoms were located at positions 4h (0, 0.38398, 0.5) and 4g (0.5, 0.6646, 0.5).

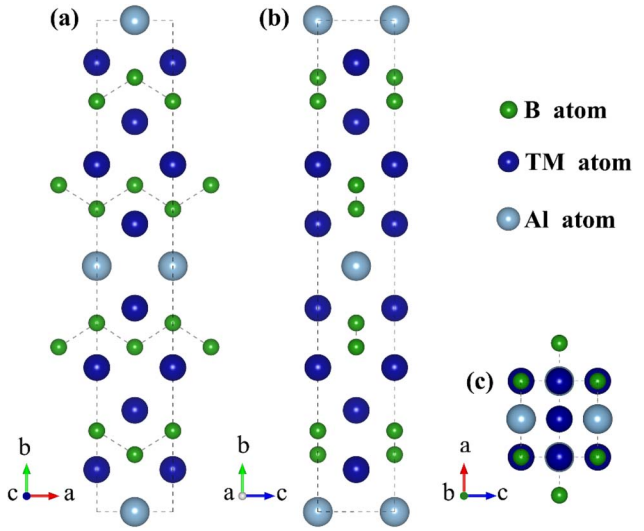

Fig. 1 Crystal structure of M_4AlB_4 (M = Cr, Mo, W), the projection of atoms on (001) (a) planes, (100) (b) planes and (010) (c) planes.

According to the crystal structure, M_4AlB_4 can be seen as M_4B_4 with Al atoms stacked in an ABABAB pattern. Normally, the interaction between M and B atoms is strong, while the interaction between M and Al atoms is weak. This crystal structure could therefore be favorable for the preparation of MABene 2D materials. Optimized structural parameters of these M_4AlB_4 tetraboride compounds are listed in Table 1, which are the same as Cr_4AlB_4 tetraboride compound experimental data and previous theoretical results.[22] Within our study, we found discrepancies between computed and empirical lattice parameters *a*, *b*, and *c* to be just 0.613%, 0.238%, and 1.244%, respectively. This shows a strong correlation between optimized Cr_4AlB_4 structural parameters and experimental data,[3] confirming the effectiveness of our computational approach in investigating M_4AlB_4 tetraboride compounds.

As a ceramic material, it is crucial for the MAB phase to present thermodynamic stability. Cohesion energy and formation enthalpy are used here to represent the thermodynamic stability of the MAB phase material. The cohesion energy and formation enthalpy of Cr_4AlB_4, Mo_4AlB_4 and W_4AlB_4 can be calculated by the following equations:[10,31,32]

$$E_c(M_4AlB_4) = \frac{1}{9}[4E_{iso}(M) + E_{iso}(Al) + 4E_{iso}(B) - E(M_4AlB_4)] \quad (1)$$

Table 1 Calculated structural parameters (*a*, *b* and *c* in Å), formation enthalpy ΔH (in eV per atom) and cohesive energy E_c (in eV per atom) for M_4AlB_4 (M = Cr, Mo, W)

	Lattice parameters (Å)				
	a	*b*	*c*	ΔH	E_c
Cr_4AlB_4	2.916	18.846	2.936	−0.516	8.055
Cr_4AlB_4 (ref. 19)	2.932	18.911	2.952		
Cr_4AlB_4 (ref. 22)	2.934	18.891	2.973		
Mo_4AlB_4	3.090	19.975	3.166	−0.490	8.699
W_4AlB_4	3.102	19.986	3.174	−0.336	9.267

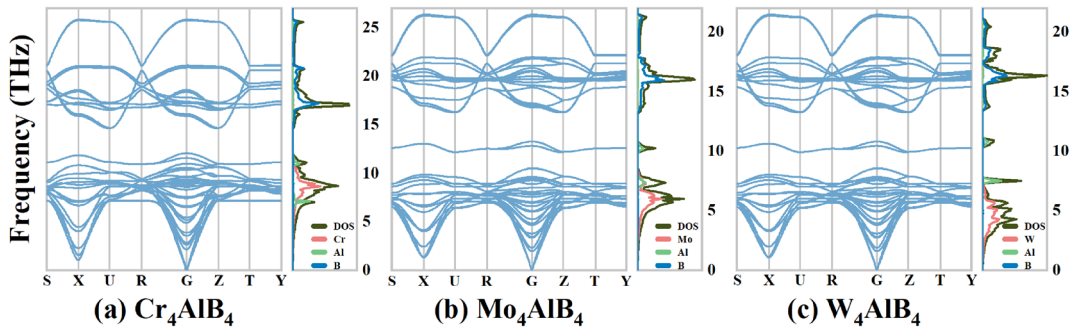

Fig. 2 Phonon dispersion curves and phono density of state for (a) Cr_4AlB_4, (b) Mo_4AlB_4 and (c) W_4AlB_4.

$$\Delta H(M_4AlB_4) = \frac{1}{9}[E(M_4AlB_4) - 4E_{bulk}(M) - E_{bulk}(Al) - 2E(B_2)] \quad (2)$$

In eqn (1) and (2), $E(M_4AlB_4)$ (M = Cr, Mo, W) and $\Delta H(M_4AlB_4)$ are cohesive energy and formation enthalpy, respectively. E_{iso} represents the energy of an atom in an isolated state, which is usually obtained by placing the atom in a 15 × 15 × 15 (Å) lattice. $E_c(M_4AlB_4)$ represents the cohesion energy. The energy of each atom in the bulk state is represented by E_{bulk}, often expressed as the energy of each atom in a simple substance, where $E(B_2)$ is the energy of a single crystal of boron. Regularly, the more negative of the cohesion energy and formation enthalpy, the more stable the material is. With a focus on energy, both E_c and ΔH are negative, indicating that these substances can be stabilized. Meanwhile, $\Delta H(Cr_4AlB_4) < \Delta H(Mo_4AlB_4) < \Delta H(W_4AlB_4)$, indicating that Cr_4AlB_4 is thermodynamically more stable compared to Mo_4AlB_4 and W_4AlB_4, therefore Cr_4AlB_4 can be more easily synthesized.

The stability of three-dimensional bulk materials is governed by a combination of thermodynamics and dynamics. Furthermore, the stability of these materials can also be assessed through the examination of phonon dispersion curves. If no imaginary frequencies appear in the phonon dispersion curve, then the material is dynamically stable, otherwise it is unstable. During the research, the thermodynamic stability of these three tetraboride compounds were performed by using the PHONOPY code. Fig. 2 contains the phonon dispersion curves and phonon density of states images for M_4AlB_4 (M = Cr, Mo, W). The phonon dispersion curves of a crystal with n atoms consist of $3n$ branches, 3 of which are acoustic branches, while the remaining $3n - 3$ are optical branches. Furthermore, the phonon dispersion curves of Cr_4AlB_4, Mo_4AlB_4 and W_4AlB_4, all have non-

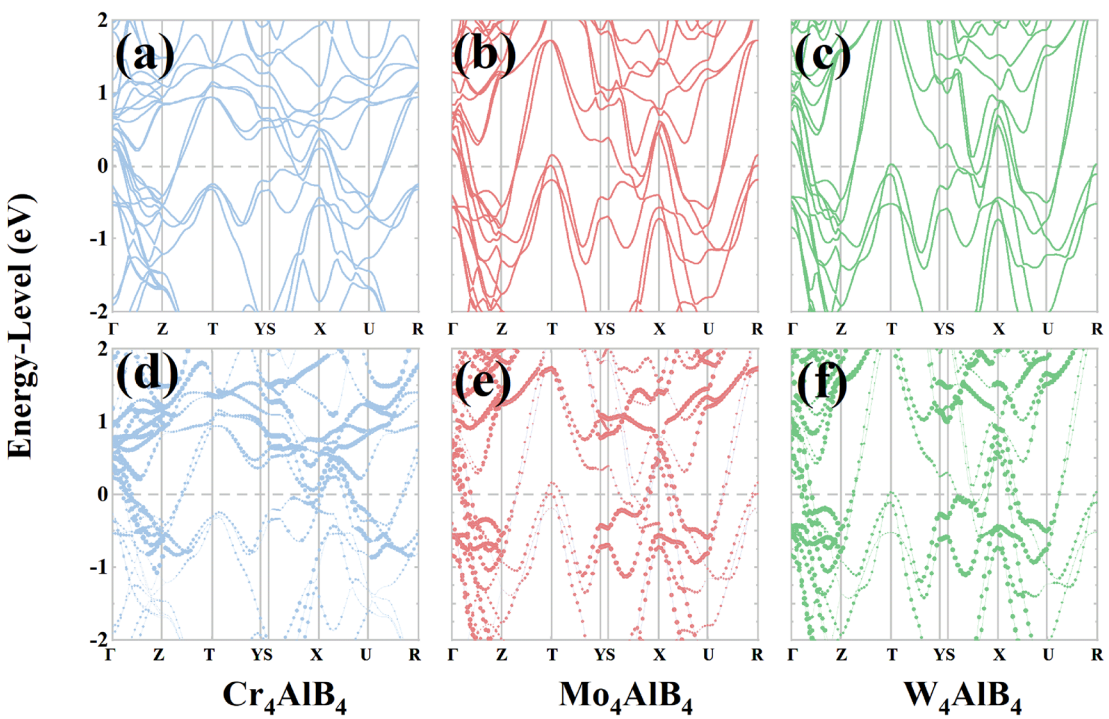

Fig. 3 Band-structures of (a) Cr_4AlB_4, (b) Mo_4AlB_4 and (c) W_4AlB_4 and projected band-structure of (d) Cr atoms in Cr_4AlB_4, (e) Mo atoms in Mo_4AlB_4 and (f) W atoms in W_4AlB_4.

zero values throughout the Brillouin zone, an indication of their stability in molecular dynamics.[33] The phonon density of states corresponds to the phonon dispersion curves, which indicates the high accuracy of the calculated results. Besides, from Fig. 2, the contribution of B atoms in Cr_4AlB_4 to the phonon density of states is concentrated in the high frequency region. The contribution of Cr and Al atoms to the phonon density of states is concentrated in the low-frequency region. It is probably related to the mass of the atoms, where the lighter masses are more likely to vibrating at high frequencies, while the larger masses tend to vibrate at low frequencies.[17,34] The similar situation is also seen in the phonon dispersion curves of two tetraborides, Mo_4AlB_4 and W_4AlB_4. Furthermore, the phonon density of states reflects an increasing contribution of Mo and W atoms with increasing atomic mass in the lower frequency region. More interestingly, Al atoms behave more like separate atoms in these tetraborides. The optical branch of Al atoms appears mainly at 10 THz in phonon density of states, while the acoustic expenditure appears at 7–7.5 THz, which is perhaps related to the weaker bonding between Al atoms and other atoms. The results mean that Mo_4AlB_4 and W_4AlB_4 may be able to prepare the corresponding MABene materials easier.

3.2. Electronic structures

Here, the electronic structures of three tetraborides are investigated by bands-structures, projected band-structure, density of states (DOS) and partial density of states (PDOS). Fig. 3 depicts the bands-structures, projected band-structure of Cr_4AlB_4, Mo_4AlB_4 and W_4AlB_4, where the Fermi energy levels of these compounds are indicated by the dashed 0-scale lines. From Fig. 3, it can be seen that the valence and conduction bands of these compounds span the Fermi energy level, indicating conductor-like properties typical of metallic ceramics. The presence of this energy band structure is due to the orbital hybridization of M atoms with Al and N atoms. According to the band structure diagram shown in Fig. 3, the d-orbitals of the M atoms contribute most to the bands of Cr_4AlB_4, Mo_4AlB_4 and W_4AlB_4 near the Fermi energy level, which explains their metallic properties. Meanwhile, the projected band-structure image of Cr_4AlB_4 exhibits that the Cr-3d orbital electrons are more concentrated than those of the other two tetraborides, which could have an impact on the electrical conductivity.

Fig. 4 exhibits the total and partial density of states (DOS) for Cr_4AlB_4, Mo_4AlB_4, and W_4AlB_4, where the dashed lines denote the Fermi energy level. The DOS plots reveal non-zero values at the Fermi energy level, indicating the conductivity and metallic nature of these tetraborides. The partial DOS (PDOS) profiles demonstrate that the DOS of these compounds primarily originates from the M-d orbitals and the B-p orbitals, while the contribution from Al orbitals is relatively lower. This characteristic is consistent with other MAX- and MAB-phase compounds. In the energy range from −15 to −10 eV, strong

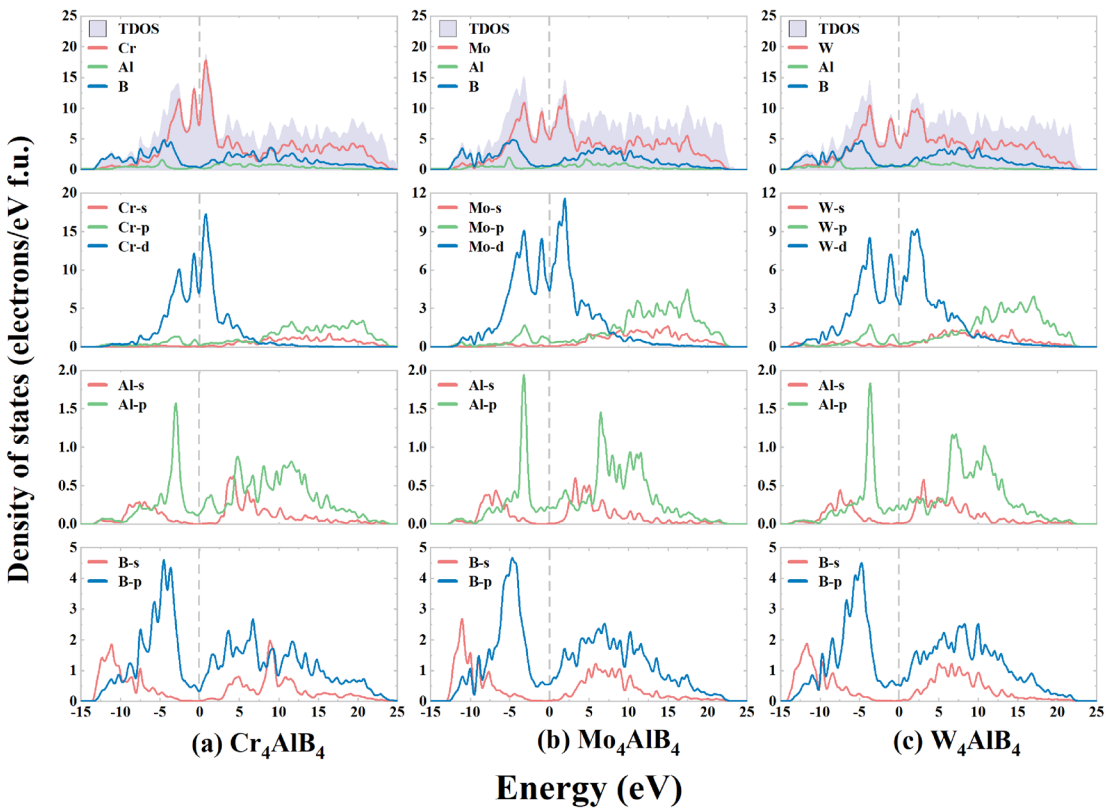

Fig. 4 DOS and PDOS of Cr_4AlB_4, Mo_4AlB_4 and W_4AlB_4.

hybridization is observed between the B-2s and the ds orbitals of the M atoms, whereas the hybridization between the Al-3s and the B-2p orbitals is less marked.

This facilitates bonding between the transition metals and B atoms, resulting in a high elastic modulus of the MAB-phase compound. In the −10 to −2 eV range, the 3d orbitals of the transition elements significantly hybridize with the B-2p orbitals. The density of states near the Fermi energy level is primarily composed of the 3d orbitals of the M elements, indicating that the conductivity of these tetraborides is mainly governed by the transition metal elements rather than Al. This conclusion aligns with the findings from the projected density of states analysis. In addition, the B-2p orbitals make a substantial contribution to the density of states near the Fermi energy level. The Al-3s and Al-3p orbitals make a relatively small contribution, mainly in the energy range of 5–25 eV. Meanwhile, COHP and IpCOHP calculations by using a Lobster code.[35,36] The calculated −pCOHP curves of Cr_4AlB_4, Mo_4AlB_4 and W_4AlB_4 are presented in Fig. 5. The COHP images of these three compounds display comparable features and all exhibit substantial bonding states. TM–Al possesses mainly bonding states, with TM–B and Al–B occupied by slightly antibonding states in proximity to the Fermi energy level. Conversely, the bonding states of the B–B bond lie above the Fermi energy level, demonstrating a noticeable degree of covalency in the B–B bond.

IpCOHP is a common method to illustrate the distinction between bonding and antibonding. It is obtained by integrating −pCOHP. Table 2 displays the results obtained from calculating IpCOHP using PBE and LDA, which reveal a similar trend across both artefacts. According to Table 2, the total IpCOHP of these compounds progressively becomes more negative as the mass of the TM atoms increases, indicating greater bonding. Consequently, both Mo_4AlB_4 and W_4AlB_4 are considered stable. The B–B bond exhibits high covalent bond strength among the compounds and has the greatest contribution to their overall bonding. On the other hand, the TM–Al bond has the least contribution to their overall bonding. Notably, the strength of the Al–B bond in Mo_4AlB_4 remains stable, but the image shows more antibonding states close to the Fermi energy level, decreasing the structural strength of Mo_4AlB_4.

Overall, the findings of COHP and IpCOHP indicate that the stability of TM_4AlB_4 grows as the mass of TM atoms increases.

Table 2 ICOHP analysis of Cr_4AlB_4, Mo_4AlB_4 and W_4AlB_4

Cr_4AlB_4		Mo_4AlB_4		W_4AlB_4		
Type	ICOHP	Type	ICOHP	Type	ICOHP	
Total	−2.107	Total	−2.440	Total	−2.518	LDA
Cr–Al	−1.151	Mo–Al	−1.545	W–Al	−1.667	
Cr–B	−1.947	Mo–B	−2.268	W–B	−2.380	
Al–B	−2.500	Al–B	−2.703	Al–B	−2.739	
B–B	−4.865	B–B	−5.216	B–B	−5.004	
Total	−1.749	Total	−1.948	Total	−2.891	PBE
Cr–Al	−1.011	Mo–Al	−1.348	W–Al	−1.423	
Cr–B	−1.766	Mo–B	−1.863	W–B	−2.177	
Al–B	−2.492	Al–B	−3.976	Al–B	−5.207	
B–B	−4.936	B–B	−4.617	B–B	−7.731	

3.3. Elastic properties

Mechanical stability plays a crucial role in assessing the stability of compounds and designing novel materials. Evaluating the

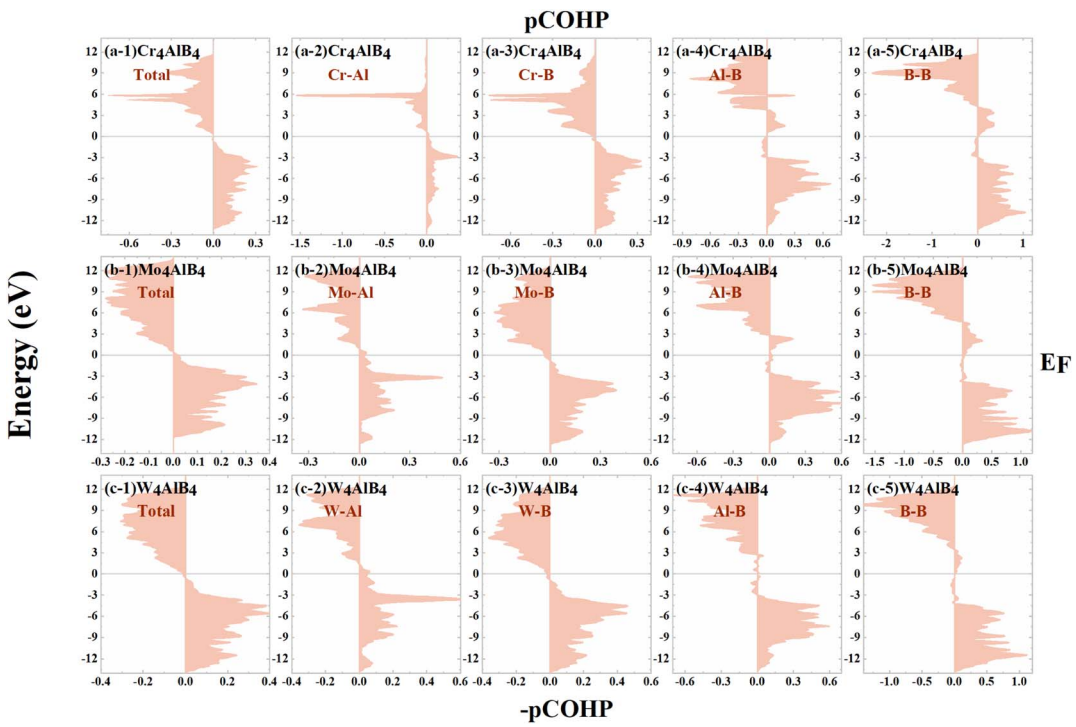

Fig. 5 The calculated −pCOHP curves of Cr_4AlB_4, Mo_4AlB_4 and W_4AlB_4.

Table 3 Calculated elastic constants C_{ij} (GPa) of Cr_4AlB_4, Mo_4AlB_4 and W_4AlB_4

M_4AlB_4	C_{11}	C_{12}	C_{13}	C_{22}	C_{23}	C_{33}	C_{44}	C_{55}	C_{66}
Cr_4AlB_4	567	116	133	492	132	481	183	241	192
Cr_4AlB_4 (ref. 19)	538	116	122	490	124	477	173	219	176
Mo_4AlB_4	529	148	162	428	158	477	152	194	136
W_4AlB_4	536	176	199	451	182	504	159	212	158

elastic constants is of significant importance. Table 3 presents the elastic constants of the investigated tetraborides, along with the corresponding results from previous studies. Elastic constants were evaluated by stress–strain method. According to the Born–Huang lattice dynamics model,[37,38] orthorhombic structures of compounds exhibit mechanical stability when the elastic constants satisfy the following criteria:

$$\begin{aligned} &C_{ij} > 0 \\ &C_{11} + C_{22} > 2C_{12} \\ &C_{11} + C33 > 2C_{13} \\ &C_{22} + C_{33} > 2C_{23} \\ &C_{12} + C_{13} + C_{33} > -2(C_{12} + C_{23} + C_{31}) \end{aligned} \tag{3}$$

As can be determined from the elastic constants in Table 3, these tetraborides meet the mechanical stability requirements. Elastic constants C_{11}, C_{22}, and C_{33} correspond to the resistance to linear compression of these compounds along the [100], [010], and [001] directions, respectively. Typically, larger elastic constants correspond to larger resistance to linear compression. Moreover, these three compounds have the largest resistance to linear compression in the [100] direction, $C_{22} > C_{33}$ in Cr_4AlB_4 single crystals and $C_{33} > C_{22}$ in Mo_4AlB_4 and W_4AlB_4 single crystals. It indicates that the resistance to linear compression of Cr_4AlB_4 is greater in the [010] direction than in the [001] direction. And the resistance to linear compression in the [001] direction is greater than that in the [010] direction in the Mo_4AlB_4 and W_4AlB_4 single crystals in the table. The C_{44} and C_{66} in the table indicate the shear stress resistance of these compounds in the (100) plane along the [001] and [110] directions. The larger values of C_{44} and C_{66} indicate the higher shear modulus of the material,[39,40] while the hardness of the material is proportional to the value of C_{44}.[39,41] According to the data in Table 3, the order of C_{44} is $Cr_4AlB_4 > W_4AlB_4 > Mo_4AlB_4$, which indicates that the highest shear modulus and hardness of Cr_4AlB_4 are the largest, and the shear modulus and hardness of Mo_4AlB_4 are the smallest, similar findings are also evident in the analysis of results from COHP and IpCHOP.

Moreover, the elastic characteristics of these tetraborides, such as the modulus as well as the Poisson's ratio ν, were obtained using the Voigt–Reuss–Hill approximation. These data were mainly calculated by the following equations:[38,42]

$$\nu = (3B_H - E)/6B_H \tag{4}$$

$$B_H = (B_V + B_R)/2 \tag{5}$$

$$G_H = (G_V + G_R) \tag{6}$$

Table 4 Calculated bulk modulus B (in GPa), shear modulus G (in GPa), Young's modulus E (in GPa), Poisson's ratio ν of Cr_4AlB_4, Mo_4AlB_4 and W_4AlB_4

M_4AlB_4	B_V	B_R	B_H	G_V	G_R	G_H	E
Cr_4AlB_4	255.7	254.7	255.2	200.6	198.0	199.3	474.4
Mo_4AlB_4	263.5	261.4	262.5	161.0	158.2	159.6	398.1
W_4AlB_4	289.7	287.6	288.7	168.0	165.1	166.6	419.1

$$E = 9B_HG_H/(3B_H + G_H) \tag{7}$$

Table 4 presents the crucial elastic properties of the investigated tetraborides. The bulk modulus B reflects the compressibility of materials under hydrostatic pressure (HP), while the shear modulus G and Youngs modulus E indicate their resistance to deformation. Generally, a high bulk modulus B signifies low compressibility, whereas a large shear modulus G indicates excellent shear resistance. Based on the data in Table 4, Cr_4AlB_4 exhibits outstanding shear resistance, whereas W_4AlB_4 demonstrates relatively good compression resistance. However, the deformation resistance of Mo_4AlB_4 is comparatively weaker.

Furthermore, the E values of these compounds are remarkably significant. Previous studies have indicated that MAX-phase materials with high E values hold great promise for thermal shock resistance.[31,43] These compounds possess structures that are similar to conventional MAX-phase materials and exhibit notable E values, making them potential candidates for thermal shock resistance.

Poisson's ratio ν and Pugh's ratio provide insights into the brittleness or ductility of solid materials. Table 5 presents the calculated Poisson's ratio ν, Pugh's ratio, and Vickers hardness of the examined tetraborides. For MAB phase compounds, a Poisson's ratio $\nu < 0.33$ and a ratio of bulk modulus to shear modulus (B/G) < 1.75 indicate brittleness, whereas values exceeding these thresholds suggest ductility.[31,44] Analysis of Table 5 reveals that these tetraborides exhibit brittleness while demonstrating excellent hardness.

Herein, it has been determined that all of these tetraborides exhibit mechanical stability. These tetraborides are potential thermal shock resistant materials. In particular, Cr_4AlB_4 has a high shear modulus and high hardness, Mo_4AlB_4 and W_4AlB_4 also have well hardness, while Mo_4AlB_4 has a more prominent damage tolerance.

3.4. Optical properties

In this section, we discuss the optical properties of Cr_4AlB_4, Mo_4AlB_4 and W_4AlB_4, mainly focusing on their response to

Table 5 Calculated Poisson's ratio ν, Pugh's ratio B/G, Vickers hardness HV (in GPa) of Cr_4AlB_4, Mo_4AlB_4 and W_4AlB_4

M_4AlB_4	ν	B/G	H_V
Cr_4AlB_4	0.19	1.28	30.15
Mo_4AlB_4	0.169	1.64	18.78
W_4AlB_4	0.26	1.73	18.02

electromagnetic waves. The calculation of the dielectric function $\varepsilon(\omega)$ of the material was employed to predict its optical properties.[45–47] The dispersion relation of the dielectric function is determined by the relationship between the transition matrix and the dielectric function. The dielectric function is obtained from the following equation:[33,44]

$$\varepsilon(\omega) = \varepsilon_1(\omega) + \mathrm{i}\varepsilon_2(\omega) \tag{8}$$

where ε_1 denotes the real part of the dielectric constant, which can be obtained by the Kramers–Kronig transformation, so that ε_1 can be calculated using the following equation:[33,44,48]

$$\varepsilon_1(\omega) = 1 + \frac{2}{\pi} P \int_0^{\infty} \frac{\omega' \varepsilon_2(\omega')}{\omega'^2 - \omega^2} \mathrm{d}\omega' \tag{9}$$

The following equation is then used to calculate the imaginary part of the dielectric function:[17,31,44]

$$\varepsilon_2(\omega) = \frac{8\pi^2 e^2}{\omega^2 m^2} \sum_n \sum_{n'} \int_{BZ} \left| P^{v}_{nn'}(k) \right|^2 f_{kn} \left(1 - f_{kn'}\right) \partial \left(E^k_n - E^k_{n'} - h\omega\right) \frac{\partial^3 k}{2\pi^3} \tag{10}$$

Table 6 Static dielectric constants $\varepsilon_1(0)$, static refractive indexes $n(0)$, static extinction coefficient $k(0)$ and reflectivity maximum R_{max} in polycrystals and principal optical axes (x, y, and z) of Cr_4AlB_4, Mo_4AlB_4 and W_4AlB_4. A_{OPT} represents anisotropy rate

Compounds		$\varepsilon_1(0)$	$n(0)$	$k(0)$	R_{max}	A_{OPT}
Cr_4AlB_4	Polycrystal	126.466	11.310	1.207	0.704	
	x	107.547	10.422	1.030	0.683	[0.850, 0.921]
	y	178.270	13.458	1.691	0.746	[1.410, 1.120]
	z	93.581	9.704	0.768	0.663	[0.740, 0.858]
Mo_4AlB_4	Polycrystal	80.277	8.988	0.711	0.641	
	x	49.513	7.041	0.245	0.566	[0.617, 0.783]
	y	128.740	11.411	1.216	0.707	[1.604, 1.300]
	z	62.578	7.923	0.451	0.603	[0.780, 0.882]
W_4AlB_4	Polycrystal	136.267	11.756	1.386	0.999	
	x	55.710	7.476	0.431	0.998	[0.409, 0.636]
	y	115.367	10.790	1.028	0.997	[0.847, 0.918]
	z	237.724	15.577	2.219	1.000	[1.745, 1.325]

The symbol f_{kn} in this equation denotes the Fermi–Dirac distribution function, m and e denote the mass of the electron and charge of an electron, respectively, $E^k_n(k)$ represents the energy that each individual electron has, while $P^{v}_{nn'}(k)$ is the projection of the elements of the momentum dipole matrix in the direction of the field v for the initial and final states.[49,50] Optical anisotropy of these tetraborides can also be calculated from the data in Table 5 by calculating the dielectric constants of the materials and also by obtaining the single-crystal and polycrystal optical properties of these materials. The optical anisotropy of a solid material can be calculated by the following equation:[44,51]

$$A_{OPT} = \left[\frac{\varepsilon_1(0)_d}{\varepsilon_1(0)_p}, \frac{n(0)_d}{n(0)_p} \right] \tag{11}$$

In the equation, $\varepsilon_1(0)_d$, $\varepsilon_1(0)_p$, $n(0)_d$ and $n(0)_p$ are the values of $\varepsilon_1(0)$ and $n(0)$ in the direction and polycrystal, respectively. The A_{OPT} values of Cr_4AlB_4, Mo_4AlB_4 and W_4AlB_4 are calculated in Table 6. If $A_{OPT} \neq 1$, it indicates that the material exhibits optical anisotropy, otherwise it is optically isotropic. Also, the larger the A_{OPT} value from 1, *i.e.*, the larger the $|A_{OPT} - 1|$, the higher the optical anisotropy is indicated. The calculations in Table 6 exhibits that all of these tetraborides are optically anisotropic. As a whole, Cr_4AlB_4 has a smaller optical anisotropy, whereas W_4AlB_4 has a larger optical anisotropy.

In addition, it is worth noting that the R_{max} value of W_4AlB_4 is very high, which indicates that W_4AlB_4 is extremely reflective of light at certain wavelengths. Fig. 6 plots the reflectance spectra of Cr_4AlB_4, Mo_4AlB_4 and W_4AlB_4. When the incident photon energy has multiple peaks in the 0–100 eV range, the peaks for Cr_4AlB_4, Mo_4AlB_4 and W_4AlB_4 are 0.704, 0.640, and 0.999 respectively. For the polycrystalline Cr_4AlB_4 and Mo_4AlB_4, the highest reflectivity was observed at 0 eV with R_{max} values of 0.704 and 0.641 respectively. The results indicate that for the polycrystalline Cr_4AlB_4 and Mo_4AlB_4, they have relatively high reflectance in the far-infrared spectral region. This is similar to most of the MAB or MAX phase materials which appear to be relatively common. In contrast, W_4AlB_4 also performs relatively normally for light in the 0–20 eV range. However, it is surprising that W_4AlB_4 has a significantly higher reflectance (above 80%) for light from 19.84–23.6 nm, which is even more surprising

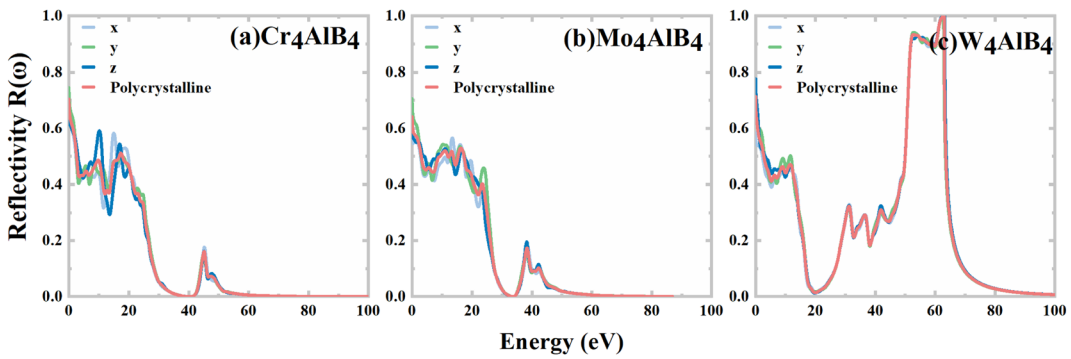

Fig. 6 Reflectivity $R(\omega)$ of (a) Cr_4AlB_4, (b) Mo_4AlB_4 and (c) W_4AlB_4.

than the previously reported MAX phase compound. The higher reflectance indicates that W_4AlB_4 is a promising new material with a strong reflection effect on EUV region. Potential applications include reflective coatings for EUV lithography equipment and EUV imaging telescopes.

4. Conclusion

In this work, we comprehensively examine the phononic, electronic, elastic, and optical properties of Cr_4AlB_4, Mo_4AlB_4, and W_4AlB_4 compounds. The results we derived affirm the remarkable stability of them in terms of energy considerations, dynamic stability, and mechanical robustness. We quantified the dielectric constants $\varepsilon_1(0)$ to be 126.466, 80.277, and 136.267 for Cr_4AlB_4, Mo_4AlB_4, and W_4AlB_4, respectively. Of noteworthy significance, W_4AlB_4 exhibits particularly weakened bonds between aluminum and B atoms, positioning it as an appropriate precursor material for two-dimensional MABene structures. Furthermore, Cr_4AlB_4 and W_4AlB_4 display elevated hardness and shear modulus, imparting them with the potential to function as materials resilient against thermal shocks. On the other hand, Mo_4AlB_4 shows enhanced damage tolerance. Optically, these compounds manifest optical anisotropy. Among them, W_4AlB_4 exhibits the most pronounced anisotropic behavior. Particularly striking is, W_4AlB_4 exceptional optical response to light within the wavelength span of 19.84–23.6 nm, rendering it an ideal contender for EUV reflective coatings.

Conflicts of interest

There are no conflicts to declare.

Acknowledgements

This work was financially supported by the National Natural Science Foundation of China (NSFC) (Grant No. 62204270, 62104073) and Middle-Young Teacher Education Research Project of Fujian Province (Grant No. JAT220020). We thank Professor Yulei Han for his assistance in theoretical calculations.

References

1 X. F. Hao, Y. H. Xu, Z. J. Wu, D. F. Zhou, X. J. Liu, X. Q. Cao and J. Meng, *Phys. Rev. B: Condens. Matter Mater. Phys.*, 2006, **74**, 224112.
2 H. Y. Chung, M. B. Weinberger, J. B. Levine, A. Kavner, J. M. Yang, S. H. Tolbert and R. B. Kaner, *Science*, 2007, **316**, 436–439.
3 H. M. Zhang, H. M. Xiang, F. Z. Dai, Z. L. Zhang and Y. C. Zhou, *J. Mater. Sci. Technol.*, 2018, **34**, 2022–2026.
4 E. J. Zhao, J. A. Meng, Y. M. Ma and Z. J. Wu, *Phys. Chem. Chem. Phys.*, 2010, **12**, 13158–13165.
5 J. J. Li and F. L. Deepak, *Chem. Rev.*, 2022, **122**, 16911–16982.
6 Y. Cheng, H. Wang, H. Song, K. Zhang, G. I. N. Waterhouse, J. Chang, Z. Tang and S. Lu, *Nano Research Energy*, 2023, **2**, e9120082.
7 M. Zhang, N. Liang, D. Hao, Z. Chen, F. Zhang, J. Yin, Y. Yang and L.-s. Yang, *Nano Research Energy*, 2023, **2**, e9120077.
8 A. Rosenkranz, D. Zambrano, A. Przyborowski, R. Shah and A. Maria Jastrzebska, *Adv. Mater. Interfaces*, 2022, **9**, 2200869.
9 H. Zhang, J. Y. Kim, R. Su, P. Richardson, J. Xi, E. Kisi, J. O'Connor, L. Shi and I. Szlufarska, *Acta Mater.*, 2020, **196**, 505–515.
10 Y. Sun, A. Yang, Y. Duan, L. Shen, M. Peng and H. Qi, *Int. J. Refract. Met. Hard Mater.*, 2022, **103**, 105781.
11 X. Lu, S. Li, W. Zhang, B. Yao, W. Yu and Y. Zhou, *J. Eur. Ceram. Soc.*, 2019, **39**, 4023–4028.
12 V. Natu, S. S. Kota and M. W. Barsoum, *J. Eur. Ceram. Soc.*, 2020, **40**, 305–314.
13 W. G. Fahrenholtz, G. E. Hilmas, I. G. Talmy and J. A. Zaykoski, *J. Am. Ceram. Soc.*, 2007, **90**, 1347–1364.
14 M. M. Opeka, I. G. Talmy and J. A. Zaykoski, *J. Mater. Sci.*, 2004, **39**, 5887–5904.
15 D. M. Van Wie, D. G. Drewry, D. E. King and C. M. Hudson, *J. Mater. Sci.*, 2004, **39**, 5915–5924.
16 B. Li, Y. Duan, L. Shen, M. Peng and H. Qi, *Philos. Mag.*, 2022, **102**, 1628–1649.
17 M. Zou, L. Bao, A. Yang, Y. Duan, M. Peng, Y. Cao and M. Li, *J. Mater. Res.*, 2023, **38**, 1396–1409.
18 Z. Jiang, P. Wang, X. Jiang and J. Zhao, *Nanoscale Horiz.*, 2018, **3**, 335–341.
19 F.-Z. Dai, H. Zhang, H. Xiang and Y. Zhou, *J. Mater. Sci. Technol.*, 2020, **39**, 161–166.
20 A. Carlsson, J. Rosen and M. Dahlqvist, *Phys. Chem. Chem. Phys.*, 2022, **24**, 11249–11258.
21 J. Zhou, J. Palisaitis, J. Halim, M. Dahlqvist, Q. Tao, I. Persson, L. Hultman, P. O. A. Persson and J. Rosen, *Science*, 2021, **373**, 801–805.
22 H. M. Zhang, F. Z. Dai, H. M. Xiang, Z. L. Zhang and Y. C. Zhou, *J. Mater. Sci. Technol.*, 2019, **35**, 530–534.
23 G. Kresse and J. Furthmuller, *Phys. Rev. B: Condens. Matter Mater. Phys.*, 1996, **54**, 11169–11186.
24 G. Kresse and J. Furthmuller, *Comput. Mater. Sci.*, 1996, **6**, 15–50.
25 W. Kohn and L. J. Sham, *Phys. Rev.*, 1965, **140**, A1133–A1138.
26 P. Wang, Y. Chu, A. Tudi, C. W. Xie, Z. H. Yang, S. L. Pan and J. J. Li, *Adv. Sci.*, 2022, **9**.
27 L. Luo, L. Wang, J. Chen, J. Zhou, Z. Yang, S. Pan and J. Li, *J. Am. Chem. Soc.*, 2022, **144**, 21916–21925.
28 J. Z. Zhou, Z. X. Fan, K. W. Zhang, Z. H. Yang, S. L. Pan and J. J. Li, *Mater. Horiz.*, 2023, **10**, 619–624.
29 J. P. Perdew, K. Burke and M. Ernzerhof, *Phys. Rev. Lett.*, 1996, **77**, 3865–3868.
30 A. Togo and I. Tanaka, *Scr. Mater.*, 2015, **108**, 1–5.
31 A. Yang, Y. Duan, L. Bao, M. Peng and L. Shen, *Vacuum*, 2022, **206**, 111497.
32 C. J. Bartel, *J. Mater. Sci.*, 2022, **57**, 10475–10498.
33 Y. Lu, A. Yang, Y. Duan and M. Peng, *Vacuum*, 2021, **193**, 110529.
34 Y. Pan, X. H. Wang, S. X. Li, Y. Q. Li and M. Wen, *RSC Adv.*, 2018, **8**, 18008–18015.
35 R. Dronskowski and P. E. Blochl, *J. Phys. Chem.*, 1993, **97**, 8617–8624.

36 S. Steinberg and R. Dronskowski, *Crystals*, 2018, **8**.
37 I. Waller, *Acta Crystallogr.*, 1956, **9**, 837–838.
38 A. C. Yang, Y. H. Duan, J. H. Yi and C. J. Li, *Chem. Phys. Lett.*, 2021, **783**, 139088.
39 A. Yang, L. Bao, M. Peng and Y. Duan, *Mater. Today Commun.*, 2021, **27**, 102474.
40 Y. Q. Qiao, K. W. Zheng and X. P. Guo, *Surf. Eng.*, 2019, **35**, 588–595.
41 H. Zhu, L. Shi, S. Li, S. Zhang and W. Xia, *Int. J. Mod. Phys. B*, 2018, **32**, 1850120.
42 R. F. Wang, A. C. Yang, L. K. Bao, M. J. Peng and Y. H. Duan, *Vacuum*, 2022, **202**, 111146.
43 Y. Zhou, H. Xiang, F.-Z. Dai and Z. Feng, *J. Mater. Sci. Technol.*, 2018, **34**, 1441–1448.
44 Y. H. Duan, L. S. Ma, P. Li and Y. Cao, *Ceram. Int.*, 2017, **43**, 6312–6321.
45 Z. Chen, Q. Chen, Z. Chai, B. Wei, J. Wang, Y. Liu, Y. Shi, Z. Wang and J. Li, *Nano Res.*, 2022, **15**, 4677–4681.
46 Z. X. Chen, S. Chu, J. P. Chen, H. Chen, J. T. Zhang, X. Z. Ma, Q. G. Li and X. C. Chen, *Nano Energy*, 2019, **56**, 294–299.
47 T. Li, Y. Zhu, X. Ji, W. Zheng, Z. Lin, X. Lu and F. Huang, *J. Phys. Chem. Lett.*, 2020, **11**, 8901–8907.
48 X. Z. Gao, Q. Chen, Q. G. Qin, L. Li, M. Z. Liu, D. Hao, J. J. Li, J. B. Li, Z. C. Wang and Z. X. Chen, *Nano Res.*, 2023, **15**, 5933–5939.
49 T. Li, M. Wang, X. Liu, M. Jin and F. Huang, *J. Phys. Chem. Lett.*, 2020, **11**, 2402–2407.
50 J. Li, Z. Lian, Q. Li, Z. Wang, L. Liu, F. L. Deepak, Y. Liu, B. Li, J. Xu and Z. Chen, *Nano Res.*, 2022, **15**, 5933–5939.
51 D. Y. Qu, L. K. Bao, Z. Z. Kong and Y. H. Duan, *Vacuum*, 2020, **179**, 109488.